Nucl. Phys. B 1025 (2026) 117402

Contents lists available at ScienceDirect

Nuclear Physics, Section B

journal homepage: www.elsevier.com/locate/nuclphysb

High Energy Physics - Theory

Holographic Krylov complexity for conformal quiver gauge theories

Ali Fatemiabhari [a,b], Horatiu Nastase [c], Carlos Nunez [b,*], Dibakar Roychowdhury [d]

[a] Institute for Theoretical and Mathematical Physics, Lomonosov Moscow State University, 119991, Moscow, Russia
[b] Department of Physics, Centre for Quantum Fields and Gravity, Swansea University, Swansea, SA2 8PP, United Kingdom
[c] Instituto de Física Teórica, UNESP-Universidade Estadual Paulista R, Dr. Bento T. Ferraz 271, Bl. II, Sao Paulo, SP, 01140-070, Brazil
[d] Department of Physics, Indian Institute of Technology Roorkee, Roorkee, Uttarakhand, 247667, India

ARTICLE INFO

Editor: Y Lozano

Keywords:
AdS/CFT
Complexity.

ABSTRACT

We investigate holographic Krylov complexity in fully top-down AdS_3 and AdS_2 supergravity backgrounds dual to two-dimensional linear-quiver SCFTs and one-dimensional conformal quantum mechanics. In these geometries, the warp factors, dilaton and other fields depend non-trivially on the 'quiver coordinate' (denoted by η in this paper). This η-coordinate encodes the color and flavor data of the dual theories. As a consequence, a massive probe following a holographic geodesic necessarily moves simultaneously in the radial AdS direction and along the 'quiver direction'. This produces new contributions to the proper momentum and hence to the rate of Krylov complexity growth, which is absent in bottom-up AdS models. We show that the η-motion is generically damped, with a time-scale governed by the UV cutoff of the geodesic problem, and modifies the early-time evolution of complexity in a quiver-dependent way. At late times, the η-dynamics freezes and the growth becomes universal, matching pure Poincare AdS predictions. Studying Abelian and non-Abelian T-dual backgrounds of $AdS_3 \times S^3 \times T^4$, quivers with localized flavor groups, and quivers with smeared flavor groups, we quantify how quiver parameters shape the operator-spreading dynamics. Our results provide a systematic characterization of Krylov complexity in top-down AdS_3/AdS_2 duals and reveal a holographic mechanism through which complexity probes both ultraviolet quiver structure and emergent infrared universality

1. Introduction and general idea

Krylov complexity has recently emerged as a powerful diagnostic of operator growth in quantum many-body systems. In holographic settings, it has been argued that the rate of growth of Krylov complexity is encoded geometrically in the proper momentum of a bulk particle following a radial geodesic, see for example [1–4]. This relation was proposed in JT gravity and in the double-scaled SYK model, see [5–9] and the reviews [10–12].

More recently, the authors of [13] proposed a concrete formulation in AdS backgrounds in which the time derivative of the complexity is directly proportional to the proper momentum of a massive probe falling along the AdS radial direction $\bar{\rho}$. The precise

* Corresponding author.
E-mail address: c.nunez@swansea.ac.uk (C. Nunez).

https://doi.org/10.1016/j.nuclphysb.2026.117402
Received 16 January 2026; Received in revised form 5 March 2026; Accepted 11 March 2026
Available online 21 March 2026

relation is

$$\dot{C}(t) = -\frac{P_{\tilde{\rho}}}{\epsilon} \,, \tag{1.1}$$

with ϵ an UV regulator. The definition of Krylov complexity was later extended to supersymmetric theories, and semiclassical strings in a gravity dual in [14].

In [15], the notion of proper momentum and proper coordinates was generalised to the case of AdS_5 (dual to $\mathcal{N} = 4$ SYM) sliced by AdS_3, in order to calculate the evolution of holographic Krylov complexity in $\mathcal{N} = 4$ SYM. A further step was taken in [16], where these notions are extended to the case of confining gauge theories with top-down string duals.

The purpose of this paper is to take an essential next step: to analyze holographic Krylov complexity in fully top-down constructions of AdS_3 and AdS_2 geometries, where the dual field theories are supersymmetric quiver gauge theories in two and one dimensions. See the papers [17–21] for AdS_3 and [22–24] for AdS_2. We refer to our calculation as Krylov complexity because it is the natural generalisation of that in [13] in our case, enriched by warp factors that make our backgrounds dual to conformal quiver gauge theories.

These quivers are highly structured interacting field theories that flow to conformal fixed points in the IR and whose holographic duals are warped AdS backgrounds with nontrivial dependence on an internal η-coordinate. This coordinate encodes the "linear quiver" or "field theory" direction and is determined by piecewise linear functions $h_4(\eta)$ and $h_8(\eta)$ that act as rank functions for the gauge groups and flavor content of the dual SCFT (they also encode the Hanany-Witten set up [25]). Such solutions preserve four Poincaré supercharges and exhibit an $SU(2)$ R-symmetry.

A key observation of this work is that the evolution of holographic Krylov complexity in these top-down geometries cannot be captured by the AdS radial direction alone. Because the warp factors and dilaton depend non-trivially on the quiver coordinate η, the geodesic of a massive particle necessarily involves simultaneous motion in both $r(t)$ and $\eta(t)$, except for a few and finely-tuned choices of h_4, h_8 rank functions. Consequently, the proper momentum–and therefore the rate of Krylov complexity growth–acquires contributions from the quiver dynamics. This qualitatively novel feature distinguishes top-down constructions from the effective AdS models studied in [13] and other papers.

In other words, for bottom-up AdS treatments, the proper momentum and therefore the complexity growth, comes solely from radial infall. However, in the (top-down) supergravity backgrounds dual to 2d and 1d linear-quiver SCFTs, the metric and dilaton depend on the η-coordinate in such a way that a particle cannot fall purely radially unless the rank functions take very special forms. The equations of motion force a nonzero $\eta(t)$. This means that the particle explores both the renormalization-group r-direction and the quiver η-direction simultaneously. Physically, this reflects a simple fact: operator growth in a linear quiver CFT inevitably spreads across gauge nodes, because bifundamental matter dynamically couples all nodes. The holographic dual encodes this "spreading" in the warping functions.

We show that the motion in the η-direction is generically damped and controlled by the UV cutoff scale introduced in the geodesic problem. At early times, the particle explores the quiver direction, and the Krylov complexity receives quiver-dependent corrections. At late times, the η-motion freezes, and the complexity growth becomes indistinguishable from that of pure Poincaré AdS, in agreement with the bottom-up proposal. The UV quiver data influences the initial stages of operator growth, while at long times the dynamics averages over the quiver structure and flows to the one of universal CFTs.

We illustrate these effects across several families of supergravity solutions: Abelian and non-Abelian T-duals of $AdS_3 \times S^3 \times T^4$, quivers with flavor groups, and quivers with smeared flavor distributions. In each case, we compute the particle trajectories $r(t), \eta(t)$, the proper momentum, and the resulting Krylov complexity. Our findings confirm that top-down holography enriches the structure of complexity growth, providing a more complete dynamical picture of how quiver degrees of freedom enhance operator spreading. These results constitute the first systematic exploration of holographic Krylov complexity in top-down AdS_3 and AdS_2 backgrounds encoding nontrivial linear quiver data.

Let us present an outline of the paper. In Section 2 we write the structure of the supersymmetric AdS_3 and AdS_2 backgrounds together with their dual quiver gauge theories. Section 3 analyses geodesic motion in these warped geometries and shows that radial infall necessarily triggers the motion along the quiver direction. In Section 4 we derive the expression for the proper momentum associated with the combined (r, η)-trajectory and explain its role in computing Krylov complexity. Section 5 contains our numerical results for several representative families of quiver CFTs and quantum-mechanical models, including Abelian and non-Abelian T-duals, quivers with localised flavor kinks, and quivers with smeared flavor distributions. For each case we determine the dynamics of $r(t)$ and $\eta(t)$, the proper momentum, and the resulting complexity growth, highlighting the influence of quiver data. Finally, Section 6 summarizes our findings and discusses future directions.

2. The supergravity backgrounds and their dual field theories

Let us start writing the supergravity backgrounds. These solutions to the equations of motion have been constructed in the framework of holographic duals to conformal field theories in diverse dimensions. Backgrounds of this type have been constructed for cases in which the dual conformal theory has at least an $SO(3)$ R-symmetry and some amount of SUSY is preserved. In this paper we focus our attention on two-dimensional CFTs and one dimensional quantum mechanical systems. We consider the case in which these systems preserve four Poincare SUSYs and have $SU(2)_R$-symmetry. The backgrounds were constructed in the papers [17–21,26], for the duals to 2d-SCFTs. For the duals to SUSY quantum mechanics, see the papers [22–24]. There are many other AdS_3 and AdS_2 backgrounds, but these are not studied here.

The AdS$_3$ backgrounds and dual SCFTs

In this work, we only need the Einstein-frame metric (as we study geodesics of particles). Other Ramond and Neveu-Schwarz fields complete these solutions of the supergravity equations of motion. For the case of backgrounds dual to 2d-SCFTs the (massive) IIA backgrounds are written in terms of three functions $h_4(\eta), h_8(\eta), u(\eta)$, with their derivatives denoted by (h_4', h_8', u'). The Einstein frame metric reads

$$\begin{aligned} ds_E^2 &= e^{-\frac{\Phi}{2}}\left[\frac{u}{\sqrt{h_4 h_8}}\left(\mathrm{d}s^2_{\mathrm{AdS}_3}+\frac{h_8 h_4}{4h_8h_4+(u')^2}\mathrm{d}s^2_{\mathrm{S}^2}\right)+\sqrt{\frac{h_4}{h_8}}\mathrm{d}s^2_{\mathrm{CY}_2}+\frac{\sqrt{h_4 h_8}}{u}\mathrm{d}\eta^2\right] \\ e^{-\Phi} &= \frac{h_8^{\frac{3}{4}}}{2h_4^{\frac{1}{4}}\sqrt{u}}\sqrt{4h_8h_4+(u')^2}. \end{aligned} \tag{2.1}$$

The background is a warped product of $\mathrm{AdS}_3\times S^2\times CY_2\times R_\eta$. The $SU(2)_R$-symmetry of the CFT is realised by the isometries of the two-sphere, the Calabi-Yau two fold plays a spectator-role and the η-coordinate is the one on which all fields and warp factors depend. In this paper we choose to write the AdS$_3$ space as

$$ds^2_{AdS_3} = e^{-\lambda r}(-dt^2+dx^2)+dr^2, \tag{2.2}$$

where λ is the inverse radius of AdS.

In [17] it was shown that the system preserves SUSY. The BPS equations and Bianchi identities for the RR-fields equations are solved if simple ordinary differential equations for $[h_4(\eta), h_8(\eta), u(\eta)]$ are satisfied. These equations read

$$\begin{aligned} h_4'' &= \textstyle\sum_{j=1}^P F_j\delta(\eta-\eta_j), \quad h_8'' = \sum_{j=1}^P \tilde{F}_j\delta(\eta-\eta_j) \\ u'' &= 0 \end{aligned} \tag{2.3}$$

In particular, the right hand side of h_4'' and h_8'' is associated with localised sources on which the Bianchi identity of the Ramond fields is violated. At those points, the background contain explicit sources. As we briefly discuss below, these localised sources provide the local $SU(F_j)$ gauge groups in the bulk that translate in the presence of global symmetries in the dual CFTs.

The functions $h_4(\eta), h_8(\eta)$ are convex polygonals. They become zero at $\eta=0$ and at $\eta=2\pi(P+1)$–which is the range of the η-coordinate. At the points η_j the polygonal changes slope and a flavour group in the CFT is generated.

The field theory dual to these backgrounds is studied in [18,19,26]. These papers write quite elaborated quivers, that in the notation customary to two-dimensional SUSY field theory contain: hypers, twisted hypers, Fermi and vector multiplets. There is an associated Hanany-Witten [25] set-up consisting of an arrangement of D2, D4, D6 and D8 branes. We do not repeat this lengthy and elaborated analysis here. The conformal field theory describes the IR-fixed point of these UV-free field theories. Various checks (gauge anomalies cancelation, global anomaly matching, central charge) have been performed, showing agreement between the field theory and the supergravity calculation. For the purposes of this paper, the reader should recall that the UV-quiver field theory is encoded in the functions h_4, h_8. These functions act as 'rank-functions' for the quiver.

For full details and clear explanations, we refer the reader to the papers [18,19,26]. Hoping to add some clarity, we write generic functions $u(\eta)$, $h_4(\eta)$ and $h_8(\eta)$ and the associated two dimensional UV-quiver field theory. Let us define

$$h_4(\eta)=\begin{cases} \frac{\beta_0}{2\pi}\eta & 0\le\eta\le 2\pi \\ \beta_0+\frac{\beta_1}{2\pi}(\eta-2\pi) & 2\pi\le\eta\le 4\pi \\ (\beta_0+\beta_1)+\frac{\beta_2}{2\pi}(\eta-4\pi) & 4\pi\le\eta\le 6\pi \\ (\beta_0+\beta_1+\ldots.+\beta_{k-1})+\frac{\beta_k}{2\pi}(\eta-2\pi k) & 2\pi k\le\eta\le 2\pi(k+1), \quad k:=3,\ldots.,P-1 \\ \alpha_P-\frac{\alpha_P}{2\pi}(\eta-2\pi P) & 2\pi P\le\eta\le 2\pi(P+1). \end{cases} \tag{2.4}$$

$$h_8(\eta)=\begin{cases} \frac{\nu_0}{2\pi}\eta & 0\le\eta\le 2\pi \\ \nu_0+\frac{\nu_1}{2\pi}(\eta-2\pi) & 2\pi\le\eta\le 4\pi \\ (\nu_0+\nu_1)+\frac{\nu_2}{2\pi}(\eta-4\pi) & 4\pi\le\eta\le 6\pi \\ (\nu_0+\nu_1+\ldots.+\nu_{k-1})+\frac{\nu_k}{2\pi}(\eta-2\pi k) & 2\pi k\le\eta\le 2\pi(k+1), \quad k:=3,\ldots.,P-1 \\ \mu_P-\frac{\mu_P}{2\pi}(\eta-2\pi P) & 2\pi P\le\eta\le 2\pi(P+1). \end{cases} \tag{2.5}$$

and

$$u=\frac{b_0}{2\pi}\eta.$$

The background in (2.1)–plus the Ramond and Neveu-Schwarz fields that we did not quote– for the functions h_4, h_8, u above is dual to the CFT describing the low energy dynamics of a two dimensional quantum field theory encoded by the quiver in Fig. 1 and the Hanany-Witten set-up of Fig. 2.

In the following we use the nomenclature for 2d multiplets in [27,28]. In these papers general aspects about 2d field theories are clearly explained and suitable to understand the field theory proposal of [18,19,26]. The papers [27,28] are recommended to the interested reader.

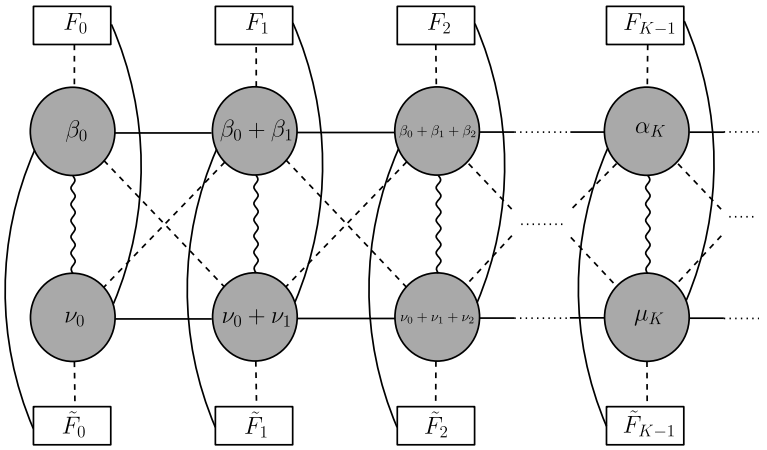

Fig. 1. A generic quiver field theory whose IR is dual to the holographic background defined by the functions in (2.4)-(2.5). The solid horizontal black line represents a $(4,4)$ twisted-hypermultiplet connecting two nearest neighbor gauge nodes. Vertically two adjacent gauge nodes are connected by $(0,4)$ hypers represented by wiggly lines and diagonally by $(0,2)$ Fermi multiplets represented by dashed lines. The solid curved lines represent $\mathcal{N}=(4,4)$ twisted hypers, connecting flavour nodes with opposite gauge nodes.

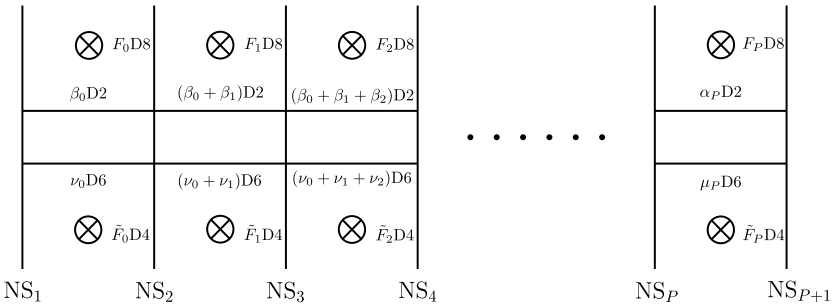

Fig. 2. Hanany-Witten set-up associated with our generic quiver in Fig. 1. The vertical lines denote NS five branes, horizontal lines D2 and D6 colour branes. The crosses, D4 and D8 flavour branes.

In the generic quiver we have two 'lines' of gauge groups, made out of $(0,4)$ vector multiplets and $(0,4)$ adjoint hypers. These nodes are horizontally joined by bifundamental matter consisting on $(4,4)$ twisted-hypermultiplets. Vertically, the gauge nodes are joined by $(0,4)$ hypers and diagonally by $(0,2)$ Fermi multiplets. There are flavour symmetries $SU(F_k)\times SU(\tilde{F}_k)$ that are joined to the adjacent gauge nodes by $(0,2)$ Fermi multiplets and with the 'opposite' gauge node by $(4,4)$ twisted hypers. This is deduced studying the string quantisation in the Hanany-Witten set-ups of Fig. 2, see [26].

The ranks of the $SU(\alpha_k)$ gauge nodes (in the upper line of the quiver) are given by $\alpha_k=\sum_{i=0}^{k-1}\beta_i$, being β_i the numbers defining the function $h_4(\eta)$. Analogously, the ranks of the $SU(\mu_k)$ gauge nodes in the lower line of the quiver are $\mu_k=\sum_{i=0}^{k-1}\nu_i$, with ν_i the numbers defining the function $h_8(\eta)$. The flavour nodes have rank $F_k=\nu_{k-1}-\nu_k$ and $\tilde{F}_k=\beta_{k-1}-\beta_k$. The papers [19,26] present detailed explanations for this proposed quivers, showing agreement for certain quantities (matching of 't Hooft anomalies, cancellation of gauge anomalies, central charges) computed both from the field theory and the supergravity pictures.

The AdS$_2$ backgrounds and dual conformal quantum mechanics:

For the AdS$_2$ Einstein frame backgrounds (dual to SUSY quantum mechanics) a very similar logic as in the AdS$_3$ case was used in their construction [22–24]. In fact, the AdS$_2$ backgrounds in [22–24] are obtained after a T-duality acting on the massive IIA backgrounds in Eq. (2.1), generating Type IIB solutions. The dual conformal quantum mechanics is proposed to be 'half' of the SCFT$_2$, in the sense of keeping only the left-sector of it. For details, see [22–24,29,30].

We quote the family of Einstein-frame metrics. These are written in terms of the AdS$_2$ of radius λ that we write in Poincare coordinates as

$$ds^2_{AdS_2}=-e^{-\lambda r}dt^2+dr^2, \tag{2.6}$$

a two sphere, a Calabi-Yau two-fold, the η-coordinate and a cyclic coordinate ψ. The same functions $[u(\eta),h_4(\eta),h_8(\eta)]$ of the form in Eq. (2.4)-(2.5) solving Eq. (2.3) are used.

$$\mathrm{d}s^2 = e^{-\frac{\Phi}{2}}\left[\frac{u}{\sqrt{h_4h_8}}\left(\frac{1}{4}\mathrm{d}s^2_{\mathrm{AdS}_2}+\frac{h_4h_8}{4h_4h_8+(u')^2}\mathrm{d}s^2_{\mathrm{S}^2}\right)+\sqrt{\frac{h_4}{h_8}}\mathrm{d}s^2_{\mathrm{CY}_2}+\frac{\sqrt{h_4h_8}}{u}(\mathrm{d}\eta^2+\mathrm{d}\psi^2)\right],$$

$$e^{-2\Phi} = \frac{h_8}{4h_4}\left(4h_4h_8 + (u')^2\right). \tag{2.7}$$

Let us close this section with an 'executive summary': we presented the metrics of families of AdS_3 backgrounds (in massive IIA) and AdS_2 in type IIB. Aside from the AdS-factor, a characteristic is the presence of an η-coordinate, ranging in $0 \le \eta \le 2\pi(P+1)$, describing a quiver with $2P$ gauge nodes, bifundamental matter and fundamental matter. The quiver is encoded in the functions $[h_4(\eta), h_8(\eta), u(\eta)]$. In some sense, the η-coordinate describes the 'field theory space'.

In the next section, we study the motion of a particle of mass m that falls under the influence of gravity along the r-coordinate. Interestingly, we *must* also allow the particle to move in the η-direction. In some sense, the geodesic explores the 'radius/energy' r-direction, and also the 'field-theory/quiver' η-direction!

3. Geodesic motion

As we anticipated, we study the motion of a particle (that couples to the Einstein frame metric), following a geodesic parametrised by the t-coordinate and $r(t), \eta(t)$. The induced metric on the particle's worldline is

$$ds^2_{ind} = e^{-\frac{\Phi}{2}} A(\eta)\left(\dot r^2 - e^{-\lambda r(t)} + \frac{\dot\eta^2}{A^2(\eta)}\right)dt^2, \quad A(\eta) = \frac{u}{\sqrt{h_4h_8}}. \tag{3.1}$$

The main difference between the metrics in Eq. (2.1) and (2.7) is in the dilaton $\Phi(\eta)$. Hence, the AdS_2 and AdS_3 cases can be dealt with simultaneously as we do in Eq. (3.1). The factor of one-quarter difference in both metrics–compare Eq. (2.1) and (2.7)– can be countered by defining in the AdS_2 case

$$r \to 2r, \quad \lambda \to \frac{\lambda}{2}\ , \ t \to 2t.$$

The action for this probe particle of mass m is

$$S = -m\int dt\sqrt{-\det[g_{ind}]} = -m\int dt\sqrt{e^{-\frac{\Phi}{2}} A(\eta)\left(e^{-\lambda r(t)} - \dot r^2 - \frac{\dot\eta^2}{A(\eta)^2}\right)}. \tag{3.2}$$

The equations of motion are

$$\frac{d}{dt}\left[\frac{e^{-\frac{\Phi}{2}} A(\eta)\,\dot r}{L}\right] = \frac{\lambda e^{-\frac{\Phi}{2}-\lambda r}\,A(\eta)}{2L}, \tag{3.3}$$

where $L = \sqrt{e^{-\frac{\Phi}{2}}\ A(\eta)\left(e^{-\lambda r} - \dot r^2 - \frac{\dot\eta^2}{A^2(\eta)}\right)}$, and

$$\frac{d}{dt}\left[\frac{e^{-\frac{\Phi}{2}}\ \dot\eta}{A(\eta)\ L}\right] = -\frac{1}{L}\left(\frac{\partial_\eta\left(e^{-\frac{\Phi}{2}} A(\eta)\right)}{2}\left[e^{-\lambda r} - \dot r^2 - \frac{\dot\eta^2}{A(\eta)^2}\right] + e^{-\frac{\Phi}{2}} \times \frac{\dot\eta^2\partial_\eta A(\eta)}{A^2(\eta)}\right). \tag{3.4}$$

The equations of motion indicate that to have constant $\eta(t) = \eta_0$, (consequently $\dot\eta = \ddot\eta = 0$), we need the derivative

$$\partial_\eta\left(e^{-\frac{\Phi}{2}} A(\eta)\right)\Big|_{\eta=\eta_0} = 0. \tag{3.5}$$

This expression (3.5) requires some qualifications. If we want that $\eta(t) = \eta_0$, with zero initial velocity $\dot\eta(0) = 0$ we must impose the value η_0 to satisfy Eq. (3.5). It could be that the solution is unstable under perturbations. These values for η_0 are *not* generic. Setting a generic η_0 as initial condition implies the motion in η does ensue (for a different take on this, see Eq. (3.15)-(3.18) below). Other possibility is to consider a generic η_0, zero initial velocity $\dot\eta(0) = 0$ but set an initial velocity $\dot r(0) = e^{-\lambda r(0)}$. This changes qualitatively the complexity and we do not consider this possibility here. Hence, for any background in which the condition in Eq. (3.5) is not satisfied, a particle moving along the r-coordinate will also necessarily move in the η-direction.

For this geodesic motion, we have a conserved Hamiltonian

$$H/m = H_0 = \frac{e^{-\lambda r - \frac{\Phi(\eta)}{4}} A(\eta)}{\sqrt{A(\eta)\left(e^{-\lambda r(t)} - \dot r^2 - \frac{\dot\eta^2}{A(\eta)^2}\right)}}. \tag{3.6}$$

From this Hamiltonian, we find

$$H_0^2\dot\eta^2 = A^2(\eta)\left[e^{-\lambda r}H_0^2 - e^{-2\lambda r - \frac{\Phi}{2}} A(\eta) - H_0^2\dot r^2\right]. \tag{3.7}$$

Using Eq. (3.7), we calculate $\ddot\eta(t)$ and replace both $\dot\eta(t)$ and $\ddot\eta(t)$ in the r-equation of motion (3.3). We find that the r-Eq. (3.3) is satisfied if

$$2e^{\lambda r}\ddot r + 2\lambda e^{\lambda r}\dot r^2 - \lambda = 0, \text{ implying}$$
$$\lambda\, r(t) = \log\left(c_1 + \frac{\lambda^2(t+c_2)^2}{4}\right). \tag{3.8}$$

Interestingly, this is the same equation that $r(t)$ would have satisfied, had we decoupled the motion from $\eta(t)$! In other words, the dynamics in $r(t)$ is the same as in pure (unwarped) AdS-spaces. This is not so surprising: we are using holography to analyse the dynamics of an operator in a two-dimensional CFT or in a conformal quantum mechanical system. Even if the theory has a quiver-like structure, it is still a CFT. What is non-trivial and new is the motion in the η-coordinate. This can be interpreted as a 'motion' along the quiver.

The integration constants c_1 and c_2 in Eq. (3.8) can be fixed from the initial conditions. We require that the particle starts its fall in the r-coordinate with zero-initial velocity, namely $\dot{r}(t=0)=0$ and with initial position equal to some large UV-cutoff position $r(t=0)=r_{UV}$. These initial conditions yield the values

$$c_1 = e^{\lambda r_{UV}} \quad \text{and} \quad c_2 = 0. \tag{3.9}$$

Substituting these values into Eq. (3.8), we find

$$\lambda\, r(t) = \log\left(e^{\lambda\, r_{UV}} + \frac{\lambda^2 t^2}{4}\right). \tag{3.10}$$

In the coordinate we used to write AdS_{d+1}, see Eq. (2.2), Eq. (2.6) and considering that $\lambda > 0$, the UV of the dual CFT is at $r \to -\infty$. So, $r_{UV} \to -\infty$ is a very negative number. The coordinate r ranges in $(-\infty_{UV}, +\infty_{IR})$. Conversely, if we choose $\lambda < 0$, then r_{UV} is very large (positive) number and the coordinate ranges in $(-\infty_{IR}, \infty_{UV})$. Then, Eq. (3.10) indicates that at $t=0$, we sit at $r = r_{UV}$, whilst as time goes by, r grows or decreases depending on the sign of λ. In fact, the time to reach $r=0$ is

$$t_f = \frac{2}{\lambda}\sqrt{1 - e^{\lambda r_{UV}}} > 0. \tag{3.11}$$

To reach $r = |r_{UV}|$ (we may call this the very far IR), the time elapsed is

$$t = \frac{\sqrt{8}}{\lambda}\sqrt{\sinh(|\lambda r_{UV}|)}. \tag{3.12}$$

Hence, the problem for the motion along the r-coordinate is solved by Eq. (3.10)–for our chosen initial conditions. Let us now study the nontrivial motion along the η-coordinate. We impose the initial conditions

$$\eta(t=0) = \eta_0 \quad \text{and} \quad \dot{\eta}(t=0) = 0, \tag{3.13}$$

using the Hamiltonian constraint in Eq. (3.7) we find

$$e^{\lambda r_{UV}} H_0^2 = A(\eta_0) e^{-\frac{\Phi(\eta_0)}{2}}. \tag{3.14}$$

We need to solve the second order equation of motion for the η-coordinate (3.4). This equation is solved if the constraint in Eq. (3.7) is satisfied and if $r(t)$ is given in Eq. (3.10). We solve for $\eta(t)$ going back to Eq. (3.7), using Eq. (3.10) for the explicit form of $r(t)$, and integrating. We find

$$\frac{H_0^2 \dot{\eta}^2}{16} = \frac{A^2(\eta)\left(A(\eta_0)e^{-\frac{\Phi(\eta_0)}{2}} - A(\eta)e^{-\frac{\Phi(\eta)}{2}}\right)}{\left(4e^{\lambda r_{UV}} + \lambda^2 t^2\right)^2} \longrightarrow \tag{3.15}$$

$$\int \frac{d\eta}{A(\eta)\sqrt{A(\eta_0)e^{-\frac{\Phi(\eta_0)}{2}} - A(\eta)e^{-\frac{\Phi(\eta)}{2}}}} = \frac{4}{H_0}\int \frac{dt}{4e^{\lambda r_{UV}} + \lambda^2 t^2}$$

$$= \frac{2e^{-\frac{\lambda r_{UV}}{2}} \arctan\left(\frac{\lambda\, t}{2} e^{-\frac{\lambda r_{UV}}{2}}\right)}{\lambda H_0}. \tag{3.16}$$

We use Eq. (3.14) to express

$$\int_{\eta_{min}}^{\eta_{max}} \frac{d\eta}{A(\eta)\sqrt{A(\eta_0)e^{-\frac{\Phi(\eta_0)}{2}} - A(\eta)e^{-\frac{\Phi}{2}}}} = \frac{2e^{-\frac{\lambda r_{UV}}{2}} \arctan\left(\frac{\lambda\, t}{2} e^{-\frac{\lambda r_{UV}}{2}}\right)}{\lambda H_0}. \tag{3.17}$$

For different quiver field theories, we have different functions $h_4(\eta), h_8(\eta)$, which produce different functions $A(\eta)$ and $e^{-\frac{\Phi(\eta)}{2}}$. The integral in Eq. (3.17)–equivalently, solving Eq. (3.15)– gives the motion along the η-coordinate as a function of time $\eta(t)$.

Typically, the integral in Eq. (3.17) cannot be solved exactly–the same goes for the ODE in Eq. (3.15). In the following sections, we perform the integral numerically, for different representative quivers and compute the complexity for these conformal quiver field theories. Before this we would like to clarify one technical point and then define the *proper momentum*.

The technical point goes as follows: from Eq. (3.15), it might seem that $\eta(t) = \eta_0$ with $\dot{\eta} = \ddot{\eta} = 0$ is a solution. On the other hand, as we observe in Eq. (3.4), keeping $\eta(t)$ fixed and $\dot{\eta}(t) = 0$ can only be attained if $\partial_\eta\left(e^{-\frac{\Phi(\eta)}{2}} A(\eta)\right) = 0$. How is that the constraint into Eq. (3.15) seems to allow for a solution with $\eta(t) = \eta_0$?

To answer this, let us study the variation of the action Eq. (3.2) respect to the constant $\eta(t)=\eta_0$ solution. That is, perform $\eta(t)=\eta_0+\delta\eta(t)$ where $\delta\eta$ is considered to be small. Keeping terms only up to second order under the square root one finds

$$S=-m\int dt$$
$$\sqrt{A(\eta_0)e^{-\frac{\Phi(\eta_0)}{2}}\left(e^{-\lambda r(t)}-\dot r^2-\frac{\delta\dot\eta^2}{A(\eta_0)^2}\right)+\partial_\eta\left[A(\eta)e^{-\frac{\Phi(\eta)}{2}}\right]\Big|_{\eta_0}\delta\eta(t)(e^{-\lambda r(t)}-\dot r^2)+\cdots}\,. \tag{3.18}$$

This contains first order terms proportional to the warping factor in the metric. This signals that constant η_0 *cannot* be a generic solution to the EOMs[1]

Let us now study the definition of the *proper momentum*, that is an instrumental quantity in the definition of the complexity.

4. Proper momentum

In this section, we will derive an expression for the proper momentum. For a geodesic that is extended in the $r(t),\eta(t)$ plane, the *proper* momentum is defined as the momentum along the proper radial direction ($\bar\rho$), which measures the distance between two points along the geodesic for a fixed time and when all the remaining coordinates are set to be constant. In the metric of AdS_3 (2.1) and AdS_2 (2.7), this corresponds to setting $\Delta t=\Delta x_i=0$ to obtain a metric in (r,η) submanifold. Here Δx_i collectively denotes all the rest of the coordinates.

Following the above definition, the proper radial distance on the geodesic connecting two points can be expressed as

$$ds_E^2\equiv d\bar\rho^2=e^{-\frac{\Phi}{2}}\left[\frac{u}{\sqrt{h_4h_8}}dr^2+\frac{\sqrt{h_4h_8}}{u}d\eta^2\right]\equiv e^{-\frac{\Phi}{2}}\left[A(\eta)dr^2+1/A(\eta)d\eta^2\right]. \tag{4.1}$$

In this section we derive an expression for the proper momentum. This is the quantity needed to compute the complexity, which is the subject of the next section. As our analysis reveals, for the most generic configuration, the Krylov complexity can be obtained through appropriate identification of the proper radial direction and the associated momentum. Let us choose the convention that λ is negative so r moves in the decreasing direction.

Since both $r(t)$ and $\eta(t)$ are functions of time, we can (in principle) invert to obtain $\eta(r)$ or $r(\eta)$. We have

$$d\bar\rho=\sqrt{e^{-\frac{\Phi}{2}}A(\eta)\left[1+\frac{1}{A(\eta)^2}\eta'(r)^2\right]}dr\to\frac{d\bar\rho}{dr}=\frac{\dot{\bar\rho}(t)}{\dot r(t)}=\sqrt{e^{-\frac{\Phi}{2}}A(\eta)\left[1+\frac{1}{A(\eta)^2}\eta'(r)^2\right]},$$
$$d\bar\rho=\sqrt{e^{-\frac{\Phi}{2}}A(\eta)\left[r'(\eta)^2+\frac{1}{A(\eta)^2}\right]}d\eta\to\frac{d\bar\rho}{d\eta}=\frac{\dot{\bar\rho}(t)}{\dot\eta(t)}=\sqrt{e^{-\frac{\Phi}{2}}A(\eta)\left[r'(\eta)^2+\frac{1}{A(\eta)^2}\right]}=$$
$$=r'(\eta)\sqrt{e^{-\frac{\Phi}{2}}A(\eta)\left[1+\frac{1}{A(\eta)^2}\eta'(r)^2\right]}. \tag{4.2}$$

We used the notation $\eta'=\frac{d\eta}{dr}$ and $r'=\frac{dr}{d\eta}$ and that $\eta'(r)=\frac{1}{r'(\eta)}$ in the very last expression of Eq. (4.2). We define the proper momentum in the $\bar\rho$ direction as

$$P_{\bar\rho}=\frac{\partial\mathcal{L}}{\partial\dot{\bar\rho}}=\frac{\partial\mathcal{L}}{\partial\dot r}\frac{\partial\dot r}{\partial\dot{\bar\rho}}+\frac{\partial\mathcal{L}}{\partial\dot\eta}\frac{\partial\dot\eta}{\partial\dot{\bar\rho}} \tag{4.3}$$
$$=\frac{P_r}{\sqrt{e^{-\frac{\Phi}{2}}A(\eta)\left[1+\frac{1}{A(\eta)^2}\eta'(r)^2\right]}}+\frac{P_\eta}{\sqrt{e^{-\frac{\Phi}{2}}A(\eta)\left[r'(\eta)^2+\frac{1}{A(\eta)^2}\right]}}.$$

Using the action in Eq. (3.2) and applying the Hamiltonian constraint in Eq. (3.6), the proper momentum simplifies considerably. In fact, we have

$$P_r=\frac{e^{-\frac{\Phi}{2}}A(\eta)\,\dot r(t)}{L}=H_0e^{\lambda r(t)}\dot r(t) \tag{4.4}$$
$$P_\eta=\frac{e^{-\frac{\Phi}{2}}A(\eta)\,\dot\eta(t)}{A(\eta)^2\,L}=\frac{H_0e^{\lambda r(t)}\dot\eta(t)}{A(\eta(t))^2}\,, \tag{4.5}$$

[1] If we expand the square-root in Eq. (3.18) we find

$$\delta S=-\frac{m}{2}\frac{e^{\frac{\Phi(\eta_0)}{2}}}{A(\eta_0)}\int dt\partial_\eta\left[A(\eta)e^{-\frac{\Phi(\eta)}{2}}\right]\Big|_{\eta_0}\delta\eta(t)+\cdots \tag{3.19}$$

where $\delta S=S/H_0-m\int dt$. The first order in $\delta\eta$ indicates that $\eta(t)=\eta_0$ is not a solution to the equations of motion.

which together with $L = \sqrt{e^{-\frac{\Phi}{2}} A(\eta)\left(e^{-\lambda r} - \dot{r}^2 - \frac{\dot{\eta}^2}{A(\eta)^2}\right)}$ gives

$$P_{\tilde{\rho}} = \frac{P_r + P_\eta \eta'(r)}{\sqrt{e^{-\frac{\Phi}{2}} A(\eta)\left[1 + \frac{1}{A(\eta)^2}\eta'(r)^2\right]}} = \frac{H_0 e^{\lambda r(t)}\dot{r}(t) + \frac{H_0 e^{\lambda r(t)}\dot{\eta}(t)}{A(\eta(t))^2}\eta'(r)}{\sqrt{e^{-\frac{\Phi}{2}} A(\eta)\left[1 + \frac{1}{A(\eta)^2}\eta'(r)^2\right]}}$$
$$= \frac{H_0 e^{\lambda r(t)}\dot{r}(t)\left(1 + \frac{\dot{\eta}(t)^2}{A(\eta(t))^2\dot{r}(t)^2}\right)}{\sqrt{e^{-\frac{\Phi}{2}} A(\eta)\left[1 + \frac{1}{A(\eta)^2}\eta'(r)^2\right]}} = \frac{H_0 e^{\lambda r(t)}\dot{r}(t)\sqrt{1 + \frac{\dot{\eta}(t)^2}{A(\eta(t))^2\dot{r}(t)^2}}}{\sqrt{e^{-\frac{\Phi(\eta(t))}{2}} A(\eta(t))}}. \tag{4.6}$$

This has a suggestive and useful form. If we impose the *constraint* $\eta = \eta_0$, we see that Eq. (4.6) gives the result of [13], rescaled by the prefactor in the AdS-metric. Once we use $r(t)$ in Eq. (3.10) and numerically solve for $\eta(t)$ using Eq. (3.15), the proper momentum is algebraically easy to obtain. Using this, we compute the complexity, in the next section. Our analysis is aligned with [13], which relates the rate of complexity growth to that with the proper momentum ($P_{\tilde{\rho}}$) along the geodesic

$$\partial_t C(t) = -\frac{P_{\tilde{\rho}}}{\epsilon}\,, \tag{4.7}$$

where ϵ plays the role of the UV cut-off. This is analogous to Eq. (1.1), borrowed from [13]. The main difference is that our proper momentum in Eq. (4.6) includes the influence of the quiver structure.

5. Numerical solutions and Krylov complexity

With the above formulation completed, the stage is now set to explore various conformal quiver field theories that are dual to backgrounds with AdS_3–see Eq. (2.1) and AdS_2–see Eq. (2.7)– factors. In the following, we discuss them under several categories. We start considering linear quivers that are holographically dual to backgrounds obtained from the well-known $AdS_3 \times S^3 \times K_3$ (or T^4) background by the application of T-duality. We continue considering the backgrounds obtained via non-Abelian T-duality from the same seed-solution. After this, we discuss more 'genuine' conformal quivers, to close with quivers in which the flavour group is 'smeared' to $U(1)^{N_f}$.

Let us discuss the physical meaning and then summarise briefly the main outcomes of the detailed numerical analysis performed in what follows.

Physical interpretation of our numerical results:

We have infinite families of SCFTs in dimensions two and one (SUSY quantum mechanics). These field theories in the UV are described by the quivers discussed in Section 2. These quivers flow to a conformal fixed point at low energies, which is what our backgrounds describe.

A scale is introduced by the UV-cutoff needed to perform the geodesic calculation. This scale separates 'early' from 'late' times. The late time behaviour for the complexity is the one found using a bottom-up approach in [13]. We observe that the probe particle moves in the η-direction (it explores the field theory direction of the quiver). The motion is heavily-damped, with a time-scale that is inverse of the UV-cutoff H_0. The early times complexity has the contribution from the η-motion (and the usual contribution from the r-motion). At late times, the geodesic motion coincides with the one found in the bottom-up approach.

The motion along the η-coordinate is the holographic expression of the fact that the operator *spreads* along the quiver. Indeed, the existence of 'bifundamental fields' (be these twisted (4,4), hypers (0,4) or Fermi multiplets) give the possibility that an operator localised on one gauge node (composed only of vector multiplets) will spread to other nodes under time evolution. This spread of the operator is generic for generic quivers, but as we discuss below there is one example in which it does not occur (Abelian T-dual of $AdS_3 \times S^3 \times T^4$). All we need is that under time evolution the mass dimension is conserved (due to the conserved Hamiltonian).

Below, we explore the influence of the quiver parameters (P, μ, ν, u_0) and the UV-cutoff H_0 on the motion, the proper momentum and on the complexity, that is always bigger than in the bottom-up approach. We observe a minimum value $\eta_{\min}$ where the η-motion stops. This value $\eta_{\min}$ depends on the quiver parameters (rank of gauge nodes) and does not seem to depend on H_0. Also, we have not observed motions across values of η where the slopes of either h_4, h_8 change. In other words, the motion is extremely damped.

Summary of the numerical results: We observe that with zero initial velocity $\dot{\eta}(0) = 0$ and for generic $\eta(0) = \eta_0$ the motion is a 'fall' towards different values of η. The motion is heavily damped. After a certain time scale, set by H_0 (or conversely r_{UV}, the scale we introduced in the problem) the motion in the η-coordinate stops. The final position $\eta(t \to \infty) = \eta_{\min}$ depends on the quiver parameters, the rank of the colour groups. The time taken to arrive to the final position (something like the half-life of the η-motion), heavily depends on H_0.

An interesting *phenomenological observation* is that the direction of motion in η depends on the rank functions h_4 and h_8. Against a naive intuition exchanging $h_4 \longleftrightarrow h_8$ changes the direction of the η-motion. This is particular to one of the quivers under study. It would be nice to have a better handle on the different aspects of the phenomenology. We leave this for future work.

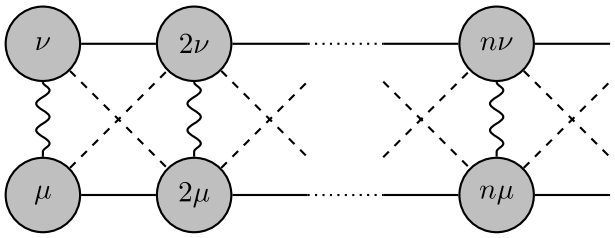

Fig. 3. Quiver associated to the NATD solution.

5.1. Example i: Abelian T-dual of $AdS_3 \times S^3 \times T^4$

The first example we choose is that of a quiver with constant rank function (since it has no kinks, there are no flavours in the quiver CFT). This is characterised by

$$h_4(\eta) = h_{4,0}, \quad h_8(\eta) = h_{8,0}, \quad u(\eta) = u_0. \tag{5.1}$$

The corresponding metric in Eq. (2.1) is the one we would have obtained by taking $AdS_3 \times S^3 \times T^4$ and performing a T-duality on a $U(1)$ inside the sphere S^3. Similarly, using Eq. (2.7) and (5.1) we find a background with an AdS_2-factor, that is the same as the one obtained after a second T-duality on AdS_3 when we write it as a the fibration over AdS_2, see [22] for details.

In this example, the massive particle trajectory is completely characterized by the radial direction $r(t)$ of AdS, while the dynamics along the quiver η-direction freezes out. Indeed, the condition in Eq. (3.5) is satisfied. This can also be seen using the constraint in the expression for $\dot{\eta}^2$ in Eq. (3.15), which yields $\eta(t) = \eta_0 =$ constant. This is a special case as the warping function of AdS-subspace is a constant, independent of η coordinate, so the AdS part is fully decoupled from the η direction and the particle trajectory is confined within AdS_3. The complexity calculation reproduces the results of [13].

It might seem obvious that the dynamics is the same as in $AdS_3 \times S^3 \times T^4$ (as the background we are working with is just the T-dual of it). But what is equivalent under T-duality is the dynamics of a string. Here we are studying the motion of a particle. As we mentioned, particles couple to the Einstein frame. It happens that Einstein and string frame in this case are equivalent, as the dilaton is constant. This is not what happens in our next example.

5.2. Example II: non-Abelian T-dual of $AdS_3 \times S^3 \times T^4$

We consider the non-Abelian T-dual of $AdS_3 \times S^3 \times T^4$ (using the left $SU(2)$ inside $SO(4)$ to perform non-Abelian T-duality) [20,31]. The dual super-conformal quiver does not contain any flavour nodes and is characterised by linearly increasing rank functions of the type

$$h_4(\eta) = \nu\eta, \quad h_8(\eta) = \mu\eta, \quad u(\eta) = u_0\eta. \tag{5.2}$$

The infinitely long quiver is plotted in Fig. 3. This is obviously not a good CFT_2; for example, the central charge diverges. How to make sense of this quiver is explained in [20,32]. For our purposes, we adopt this simple background as a proxy to calculate the complexity.

Using Eq. (5.2), it is easy to compute the functions

$$A(\eta) = \frac{u_0}{\sqrt{\mu\nu}} \tag{5.3}$$

and

$$e^{-\frac{\Phi(\eta)}{2}} = \begin{cases} \dfrac{\sqrt{\frac{(\mu)^{3/4}\sqrt{4\eta^2\mu\nu+u_0^2}}{\sqrt[4]{\nu}\sqrt{u_0}}}}{\sqrt{2}} & \text{for } AdS_3 \\ \dfrac{\sqrt{\frac{\sqrt{\mu}\sqrt{4\eta^2\mu\nu+u_0^2}}{\sqrt{\nu}}}}{\sqrt{2}} & \text{for } AdS_2. \end{cases} \tag{5.4}$$

We first provide a perturbative expansion for the $\eta(t)$ solution at early times, solving the differential Eq. (3.15),

$$\eta(t)\Big|_{t\sim 0} \sim \eta_0 - H_0^2 \frac{\eta_0 \mu^{1/8}\nu^{5/8}u_0^{5/4}}{\sqrt{2}\left(4\eta_0^2\mu\nu + u_0^2\right)^{5/4}} t^2 + O(t)^3, \tag{5.5}$$

with $\eta_0 = \eta(t=0)$. This suggests that larger H_0 leads to faster movement in the η direction in early times, while larger η_0, u_0, μ and ν lead to slower movement. For the rate of change of complexity, we have ($\lambda = -2$ is chosen)

$$\partial_t C(t)\Big|_{t\sim 0} \propto P_{\tilde{\rho}}\Big|_{t\sim 0} \sim -H_0 \frac{\sqrt[4]{2}\sqrt[16]{\mu}\nu^{5/16}\sqrt{\left(16\eta_0^4\mu^2\nu^2 + u_0^4 + 9\eta_0^2\mu\nu u_0^2\right)}}{u_0^{3/8}\left(4\eta_0^2\mu\nu + u_0^2\right)^{9/8}} t + O(t)^2, \tag{5.6}$$

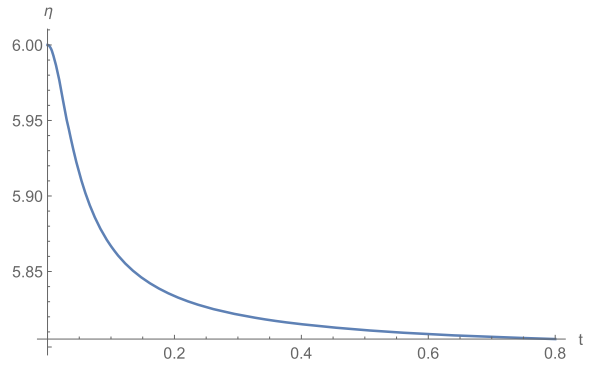

Fig. 4. The particle trajectory along the η direction for non-Abelian T-dual background. We set $\lambda = \mu = \nu = u_0 = 1$, $H_0 = 100$, $\eta_0 = 6$ and $e^{\lambda r_{UV}} = 0.00024$ is fixed by the constraint (5.8).

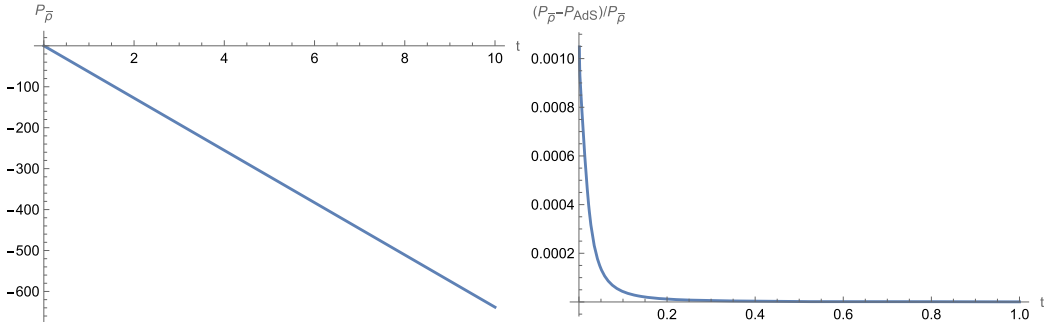

Fig. 5. Proper momentum $P_{\bar{p}}$ and its comparison with pure AdS case. $P_{\rm AdS}$ is obtained by freezing the motion in the η-direction, as indicated below Eq. (4.6). We set $\mu = \nu = u_0 = 1$, $H_0 = 100$, and $\eta_0 = 6$.

which shows the linear growth proportional to H_0. Note that the quiver parameters are clearly affecting the rate of change of the complexity.

For numerical studies the integral in Eq. (3.16) gets simplified setting $\mu = \nu = u_0 = 1$ for simplicity. It can be expressed as

$$\int_{\eta_{min}}^{\eta_0} \frac{d\eta}{A(\eta)\sqrt{A(\eta_0)e^{-\frac{\Phi(\eta_0)}{2}} - A(\eta)e^{-\frac{\Phi(\eta)}{2}}}} = \int_{\eta_{min}}^{\eta_0} \frac{d\eta}{\sqrt{e^{-\frac{\Phi(\eta_0)}{2}} - e^{-\frac{\Phi(\eta)}{2}}}}, \tag{5.7}$$

Notice that with this choice of parameters the background dilaton $e^{-\frac{\Phi(\eta)}{2}}$ is identical for both AdS_3 and AdS_2 solutions.

One can numerically solve the integral Eq. (5.7), or equivalently the differential Eq. (3.15),

$$\frac{H_0^2\dot{\eta}^2}{16} = \frac{\left[e^{-\frac{\Phi(\eta_0)}{2}} - e^{-\frac{\Phi(\eta)}{2}}\right]}{\left(\lambda^2 t^2 + 4e^{\lambda r_{UV}}\right)^2} \; ; \; e^{\lambda r_{UV}} = \frac{A(\eta_0)e^{-\frac{\Phi(\eta_0)}{2}}}{H_0^2} \; , \tag{5.8}$$

with

$$e^{-\frac{\Phi(\eta)}{2}} = \frac{\sqrt[4]{4\eta^2+1}}{\sqrt{2}} \; ; \; A(\eta) = 1.$$

The full numerical solution of $\eta(t)$ for certain choices of parameters is shown in Fig. 4 and the corresponding proper momentum and comparison with pure AdS_3 case is given in Fig. 5.

As can be seen from both Figs. 4 and 5, the particle moves in a direction of decreasing ranks of the quiver (towards $\eta \to 0$), and the momentum along the quiver coordinate (the η-coordinate) freezes out after a short period of time. The range of motion in the η direction is not considerably affected by the value of UV cut-off, H_0. As we discuss below, H_0 introduces a scale, that is inverse with the time-scale in which the η-motion is damped. The difference with the pure AdS_3 calculation is negligible at late times. Interestingly the motion along the quiver η-direction, affects the complexity only at early times, as depicted in the right panel of Fig. 5. Note that the complexity is larger than in the pure AdS case.

At late times, the momentum (and hence the Krylov complexity) receives a contribution only from the motion along AdS. This is further depicted in Fig. 5, which reveals a linear growth of complexity with time, which is in agreement with the analysis of the Poincare AdS in [13]. Let us study in more detail the parametric dependence.

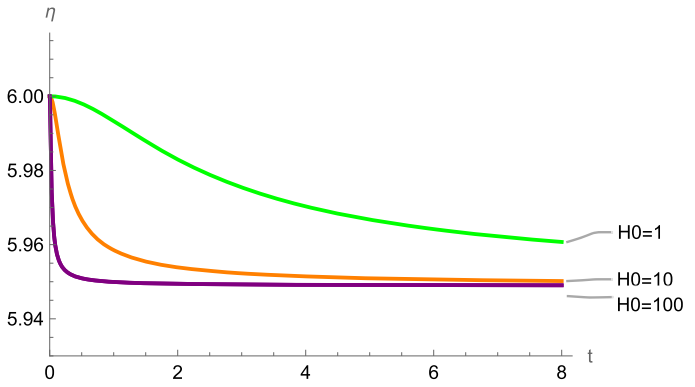

Fig. 6. The trajectory in the η direction for various H_0 choices and $u_0 = \mu = \nu = 1$.

5.2.1. Study of quiver parameters

Now, we study the effect of varying different parameters in the problem on the trajectory of the particle in the η direction. Fig. 6 shows the trajectory in example II for different H_0 choices. It is observed that the range of the motion in the η direction is not considerably affected by the value of H_0. But the rate of approach to the asymptotic value of $\eta_{\min} \equiv \eta(t \to \infty)$ is much faster for larger values of H_0.

The top and bottom panels in Fig. 7 depict the trajectory for different choices of u_0 and ν, respectively. One can see that increasing u_0 enhances the range of motion in the η direction, such that for larger values of u_0 the particle can approach the origin of the quiver direction at $\eta = 0$. The parameter ν has an inverse effect, and only for smaller values of it, the range of the motion is considerable. One should keep in mind that in the dual field theory, ν is related to the number of colours, so it should be kept large to be in a reliable gravity dual. This freezes the motion in the η direction considerably. The effect of the μ parameter is similar. One should be wary of taking (ν, μ) smaller than one, as we emphasised above. In fact, the supergravity approximation is reliable in the limit of long quivers (P large) and large ranks for each node.

Let us now study a more realistic field theory.

5.3. Example III: quivers with a kink

As our third example, we consider the effect that the flavour nodes of the quiver theory have on the complexity. We consider simple examples where the dual supergravity solutions are characterised by rank functions of the form

$$h_4(\eta) = h_{4,0}, \quad u(\eta) = u_0, \tag{5.9}$$

and

$$h_8(\eta) = \begin{cases} \frac{\nu_0}{2\pi}\eta & 0 \le \eta \le 2\pi \\ \mu_k + \frac{\nu_k}{2\pi}(\eta - 2\pi k) & 2\pi k \le \eta \le 2\pi(k+1), \quad k := 1, \dots, P-1 \\ \mu_P - \frac{\mu_P}{2\pi}(\eta - 2\pi P) & 2\pi P \le \eta \le 2\pi(P+1)\,, \end{cases} \tag{5.10}$$

where only the $h_8(\eta)$ function is introducing the flavour-nodes effects on the geometry.

The simplest situation is adding one stack of flavour branes at a certain point, namely $\eta = 2\pi P$, along the quiver axis. These "single kink" quivers are given by the following rank function

$$h_8(\eta) = \begin{cases} \frac{\mu}{2\pi}\eta, & 0 \le \eta \le 2\pi P \\ \mu P - \frac{\mu P}{2\pi}(\eta - 2\pi P), & 2\pi P \le \eta \le 2\pi(P+1). \end{cases} \tag{5.11}$$

The quiver diagram is provided in Fig. 8.

If at initial time $t = 0$, we put the particle at the position $\eta(t) = \eta_0$, in the $0 < \eta_0 < 2\pi P$, we find

$$A(\eta) = \frac{\sqrt{2\pi}}{\sqrt{\eta\mu}} \tag{5.12}$$

and

$$A(\eta) e^{-\frac{\Phi(\eta)}{2}} = \begin{cases} \frac{(\eta\mu)^{1/8}}{(2\pi)^{1/8}} & \text{for } AdS_3 \\ 1 & \text{for } AdS_2\,, \end{cases} \tag{5.13}$$

where we set $h_{4,0} = u_0 = 1$.

In what follows, we focus our analysis on AdS_3 only, as for AdS_2 the particle dynamics is decoupled from the quiver and is solely confined to AdS-spacetime. This can be seen both from Eq. (3.5) and (3.15), which yield $\dot{\eta} = 0$. With our focus now on AdS_3, the

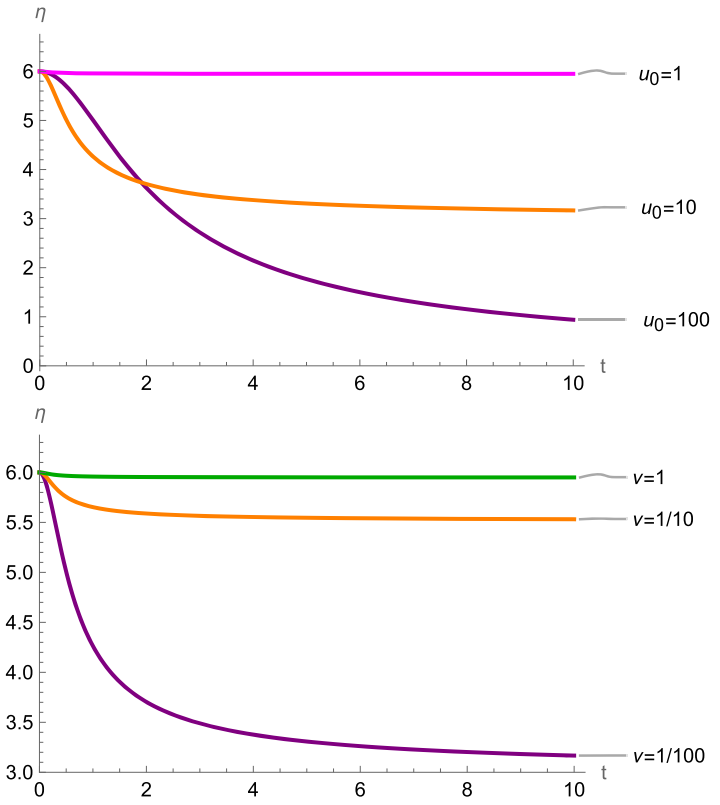

Fig. 7. The trajectory in the η direction for various u_0 choices, $\mu = \nu = 1$ (top) and various ν choices, $\mu = u_0 = 1$ (bottom) with $H_0 = 10$.

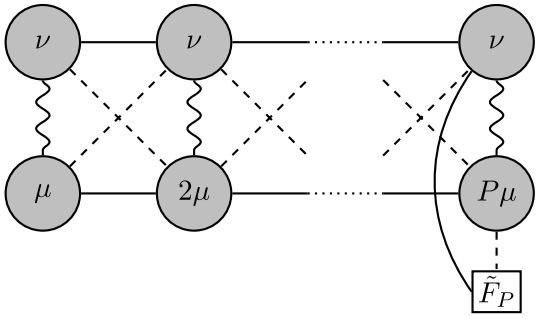

Fig. 8. Quiver associated to the example III.

corresponding integral (3.16) turns out to be

$$\int_{\eta_{min}}^{\eta_0} \frac{d\eta}{A(\eta)\sqrt{A(\eta_0)e^{-\frac{\Phi(\eta_0)}{2}} - A(\eta)e^{-\frac{\Phi(\eta)}{2}}}} = \int_{\eta_{min}}^{\eta_0} \frac{d\eta}{(2\pi)^{7/16}} \frac{\sqrt{\eta\mu}}{\sqrt{(\eta_0\mu)^{1/8} - (\eta\mu)^{1/8}}}. \tag{5.14}$$

Like the previous example, we first provide a perturbative expansion for the $\eta(t)$, in the range $0 < \eta < 2\pi P$, at early times as

$$\eta(t)\Big|_{t\sim 0} \sim \eta_0 - H_0^2 \frac{\pi^{9/8}}{8\, 2^{7/8} \eta_0^{17/8} \mu^{9/8}} t^2 + O(t)^3. \tag{5.15}$$

Here $\eta_0 = \eta(t = 0)$. This suggests that larger H_0 leads to faster movement in the η direction in early times, while larger η_0 and μ lead to slower movement. For the rate of change of complexity, we have

$$\partial_t C(t)\Big|_{t\sim 0} \propto P_{\tilde{p}}\Big|_{t\sim 0} \sim -H_0 \frac{\sqrt[16]{\pi}\sqrt{\frac{\pi}{\eta_0^3\mu} + 128}}{8 \times 2^{7/16}\, \sqrt[16]{\eta_0\mu}} t + O(t)^2, \tag{5.16}$$

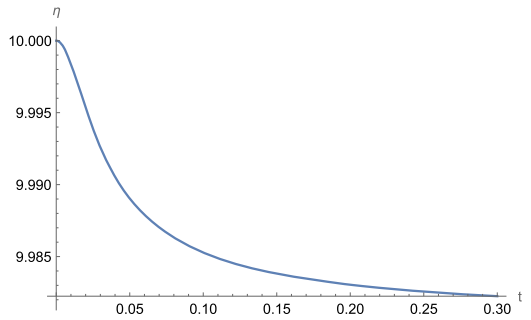

Fig. 9. The particle trajectory along the η direction for the AdS_3 case of Example III. $\eta_0 = 10$, $\mu = 1$, $H_0 = 100$ is chosen and $e^{\lambda r_{UV}} = 0.0001$ is fixed by the constraint.

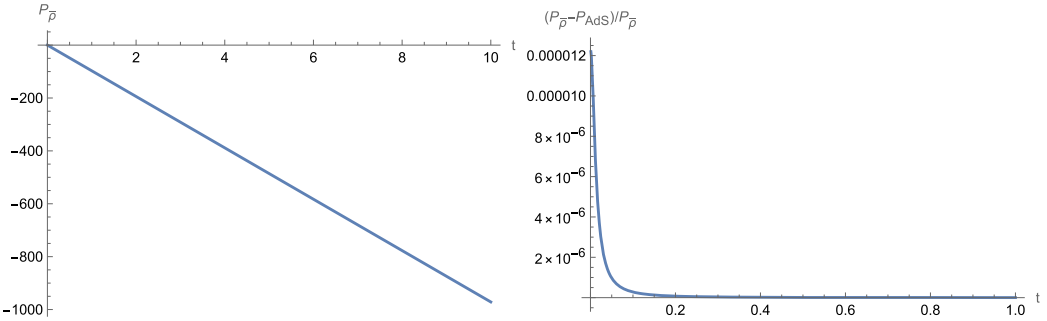

Fig. 10. Proper momentum $P_{\bar{p}}$ for the AdS_3 case and its comparison with pure AdS_3. We set $\eta_0 = 10$, $\mu = 1$, $H_0 = 100$.

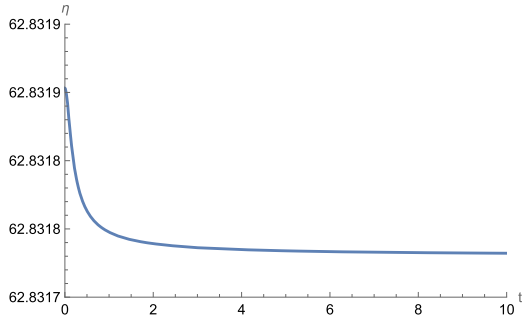

Fig. 11. The particle trajectory along the η direction for Example III. We set $\eta_0 = 2\pi P$, $P = 100$, $\mu = 1$, $H_0 = 100$.

which shows the linear growth proportional to H_0. Note that the quiver parameters are clearly affecting the rate of change of the complexity.

Like before, for the full trajectory, the integral (3.16) (or the differential Eq. (3.15)) has to be solved numerically, which yields a trajectory shown in Fig. 9. As one can see, the particle's position in η direction is decreasing, and its motion is restricted in a narrow region of $\eta_{\min} \leq \eta \leq \eta_0$, where $\eta_{\min}$ is the η-position to which the particle approaches asymptotically. In other words, the particle tends to move towards regions associated with smaller rank function values in the dual gauge theory. This is a behaviour similar to that observed in example II. The corresponding proper momentum is provided in Fig. 10.

As a further illustration of our previous calculation, we place the particle at the location of the flavour branes, namely at $\eta_0 = 2\pi P$, where we choose $P \gg 1$. We separately perform our analysis for the two intervals. For the first interval $\eta_{\min} \leq \eta \leq 2\pi P$, one gets a trajectory as shown in Fig. 11, which shows that the particle moves towards the decreasing direction of the rank function and finally stops at some $\eta = \eta_{\min}$.

For the second interval $2\pi P \leq \eta \leq 2\pi(P+1)$, we find

$$A(\eta) = \frac{\sqrt{2\pi}}{\sqrt{\mu P(\eta - 2\pi(P-1))}}\,, \tag{5.17}$$

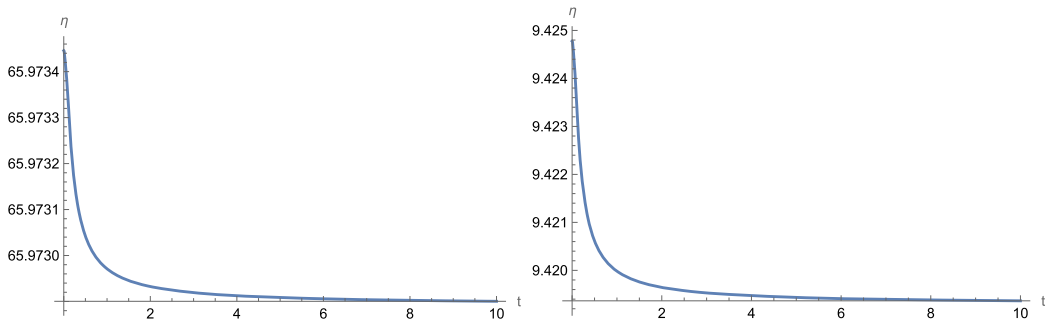

Fig. 12. The particle trajectory along the η direction for the AdS_3 case of Example III, $P = 10$ (left) and $P = 1$ (right). $\eta_0 = 2\pi(P + 1/2)$, $\mu = 1$ and $H_0 = 10$ is chosen. Note that the case $P = 1$ is done only as a sample calculation. The supergravity approximation is valid for large P.

together with the combination

$$A(\eta)e^{-\frac{\Phi(\eta)}{2}} = \begin{cases} \frac{(\mu P(\eta - 2\pi(P-1)))^{1/8}}{\sqrt[8]{2\pi}} & \text{for } AdS_3 \\ 1 & \text{for } AdS_2\,, \end{cases} \tag{5.18}$$

where we set $h_{4,0} = u_0 = 1$.

Like before, we repeat our analysis for the second interval, where we take the initial condition as $\eta_0 = 2\pi(P + 1/2)$ and set $\mu = 1$. This yields a configuration as shown in the left panel of the Fig. 12. This clearly shows that the particle always moves towards the decreasing direction of the η coordinate. Notice that, with the flavour brane located near the end of the space ($\eta_0 \sim 2\pi P \gg 1$), the particle always prefers to move in the first interval rather than the second one.

The right panel of the Fig. 12 shows the effect of the length of the quiver P on the trajectory of the particle. Lower values of P leads to larger range of motion in the η direction. But one needs to keep in mind that the supergravity solution is a reliable dual to the SCFT when P is large.

As our next example, we exchange rank functions $h_4 \leftrightarrow h_8$ and study their effect on the complexity. For the first interval $0 \le \eta \le 2\pi P$, with $\eta_0 = \eta(t = 0)$, we choose $h_8 = 1 = u$ and $h_4 = \frac{\mu}{2\pi}\eta$. This yields the functions

$$A(\eta) = \frac{\sqrt{2\pi}}{\sqrt{\eta\mu}} \tag{5.19}$$

and

$$A(\eta)e^{-\frac{\Phi}{2}} = \begin{cases} \frac{(2\pi)^{3/8}}{(\eta\mu)^{3/8}} & \text{for } AdS_3 \\ \frac{\sqrt{2\pi}}{\sqrt{\eta\mu}} & \text{for } AdS_2. \end{cases} \tag{5.20}$$

Notice that while the function $A(\eta)$ remains unchanged, the dilaton of the background is sensitive to the swapping of the rank functions, which is also evident from Eq. (2.1). In other words, the complexity would be different under the exchange of functions h_4 and h_8.

This is precisely reflected once we proceed with the numeric calculation and solve the differential Eq. (3.15). Notice that in Eq. (3.15), its right-hand side is positive definite if one satisfies $\eta(t) > \eta_0$. This produces a characteristically opposite behaviour compared to the previous cases; see Fig. 13. In other words, unlike previous cases, the particle motion tends towards a direction of increasing value of the rank function. The corresponding proper momentum is given in Fig. 14.

5.4. Example IV: Quivers with smeared flavours

As our last example, we consider quivers that are characterised by the following rank functions

$$h_4(\eta) = h_{4,0}\sin\left(\frac{\pi\eta}{P+1}\right), \quad h_8(\eta) = h_{8,0}\sin\left(\frac{\pi\eta}{P+1}\right), \quad u(\eta) = u_0. \tag{5.21}$$

This is a very peculiar situation. In fact the functions h_4, h_8 do *not* satisfy the equation of motion (2.3). One may wonder, what is the meaning of these h_4, h_8 functions. This choice indicates a smeared distribution of flavour branes. In fact, as explained in the papers [17,19], the Bianchi identity for the Ramond forms F_0 and F_4 are violated wherever h_8'' and h_4'' are nonzero. In this case, we find a continuous distribution of sources (in a different system, an example in which a continuous distribution of sources made physical sense is [33]). The η-direction ranges in $[0, (P + 1)\pi]$. We should see this example as a sample calculation.

Given (5.21), we have

$$A(\eta) = \frac{1}{\sin\left(\frac{\pi\eta}{P+1}\right)} \tag{5.22}$$

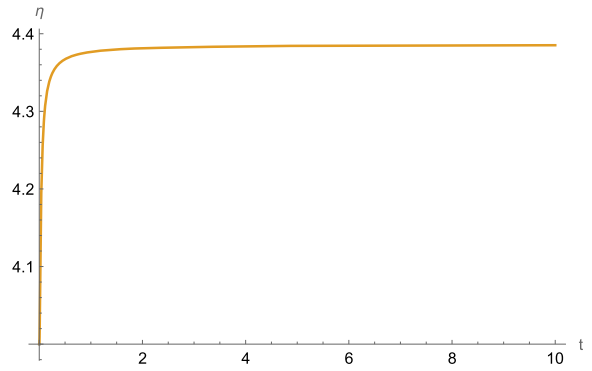

Fig. 13. The particle trajectory along the η direction for non trivial h_4 in Example III with $\eta_0 = 4$, $\mu = 1$, $H_0 = 100$.

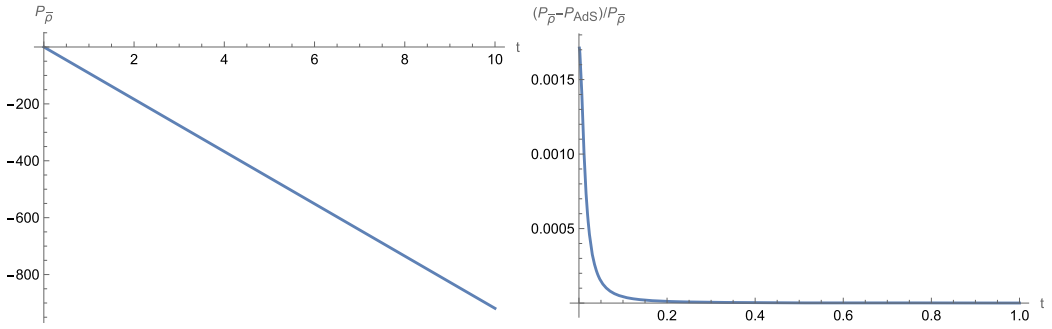

Fig. 14. Proper momentum $P_{\bar{p}}$ for non trivial h_4 and its comparison with pure AdS case. We set $\eta_0 = 4$, $\mu = 1$, $H_0 = 100$.

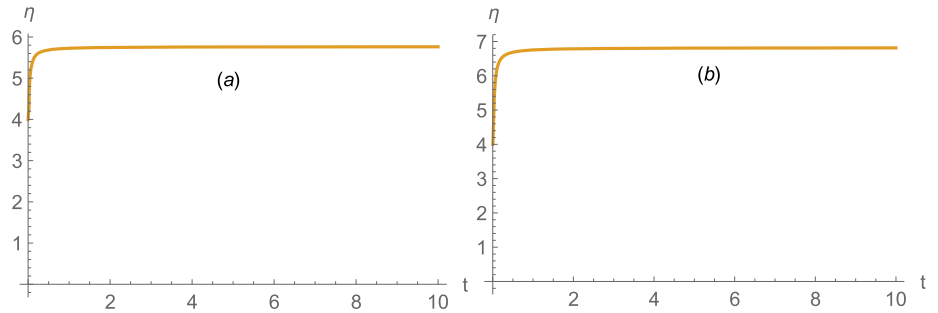

Fig. 15. The particle trajectory along the η direction for a smeared quiver in Example IV. Fig.(a) is the plot for AdS_3. We set $H_0 = 100$, $\eta_0 = 4$, $P = 50$ and $e^{\lambda r_{UV}} = 0.00014$ is fixed by the constraint (5.8). Fig.(b) is the plot for AdS_2. We set $H_0 = 100$, $\eta_0 = 4$, $P = 50$ and $e^{\lambda r_{UV}} = 0.0002$ is fixed by the constraint (5.8).

and

$$A(\eta)e^{-\frac{\Phi(\eta)}{2}} = \begin{cases} \sin^{-1/4}\left(\frac{\pi\eta}{P+1}\right) & \text{for } AdS_3 \\ \sin^{-1/2}\left(\frac{\pi\eta}{P+1}\right) & \text{for } AdS_2\,, \end{cases} \tag{5.23}$$

where we set $h_{4,0} = h_{8,0} = u_0 = 1$ for simplicity.

Next, we evaluate the integral (3.16) for AdS_3 and AdS_2 cases separately.

For AdS_3:

$$\int_{\eta_0}^{\eta_{max}} \frac{d\eta}{A(\eta)\sqrt{A(\eta_0)e^{-\frac{\Phi(\eta_0)}{2}} - A(\eta)e^{-\frac{\Phi(\eta)}{2}}}} = \int_{\eta_0}^{\eta_{max}} d\eta \frac{\sin\left(\frac{\pi\eta}{P+1}\right)\sin^{1/8}\left(\frac{\pi\eta_0}{P+1}\right)}{\sqrt{1-\frac{\sin^{1/4}\left(\frac{\pi\eta_0}{P+1}\right)}{\sin^{1/4}\left(\frac{\pi\eta}{P+1}\right)}}}. \tag{5.24}$$

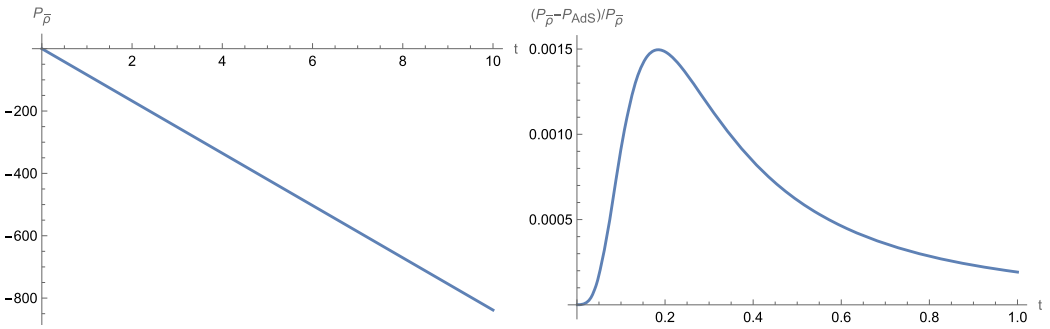

Fig. 16. Proper momentum $P_{\tilde{p}}$ and its comparison with pure AdS case for a smeared quiver with an AdS_3 factor in Example IV. We set $H_0 = 100$, $\eta_0 = 4$ and $P = 50$.

For AdS$_2$:

$$\int_{\eta_0}^{\eta_{max}} \frac{d\eta}{A(\eta)\sqrt{A(\eta_0)e^{-\frac{\Phi(\eta_0)}{2}} - A(\eta)e^{-\frac{\Phi(\eta)}{2}}}} = \int_{\eta_0}^{\eta_{max}} d\eta \frac{\sin\left(\frac{\pi\eta}{P+1}\right)\sin^{1/4}\left(\frac{\pi\eta_0}{P+1}\right)}{\sqrt{1-\frac{\sin^{1/2}\left(\frac{\pi\eta_0}{P+1}\right)}{\sin^{1/2}\left(\frac{\pi\eta}{P+1}\right)}}}. \tag{5.25}$$

The integrals in Eqs. (5.24)-(5.25) can be evaluated numerically, or instead one can solve the differential equation

$$\frac{H_0^2\dot{\eta}^2}{16} = \frac{\left[A(\eta_0)e^{-\frac{\Phi(\eta_0)}{2}} - A(\eta)e^{-\frac{\Phi(\eta)}{2}}\right]}{\sin^2\left(\frac{\pi\eta}{P+1}\right)\left(\lambda^2t^2+4c_1\right)^2}. \tag{5.26}$$

Notice that in order for the right-hand side of Eqs. (5.26) to be positive definite, one must have $\eta(t) > \eta_0$, which yields the trajectory along the η- coordinate, shown in Fig. 15. In this case, the particle moves along the direction of the increasing values of the rank function.

In Fig. 16, the proper momentum ($P_{\tilde{p}}$) is plotted which at late times has a qualitatively similar behaviour as in the case with Poincare AdS. This is reflected in the fact that the momentum of the particle along the quiver direction freezes rapidly with time and at late times its dynamics is completely characterised by the motion in AdS.

To summarise, in all four examples above, we observe a non-trivial dynamics of the probe particle along the quiver (the η-axis), either in the increasing or the decreasing direction of the values rank function. In all these cases, the motion of the particle is damped in the η direction, and as time progresses, the dynamics is fully driven by the Poincare AdS.

6. Conclusions and future work

In this work we have provided the first systematic study of holographic Krylov complexity in fully top-down AdS$_3$ and AdS$_2$ backgrounds dual to linear quiver CFTs and conformal quantum-mechanical models. Unlike effective bottom-up AdS constructions, these geometries possess a non-trivial dependence on the 'quiver field theory coordinate' (η) reflected in the rank functions h_4, h_8 that encode colour and flavour structure in the dual field theories. As a result, the motion of a massive probe particle–and hence the holographic dual of operator growth–necessarily involves simultaneous evolution in the radial direction $r(t)$ and along the 'quiver field theory direction' $\eta(t)$. We refer to our calculation as Krylov complexity, as it is a natural extension of that of [13] for the case of warp factors and quiver structures.

We showed that this produces distinctive corrections to the early-time behavior of the Krylov complexity, while at late times the η-motion is strongly damped and the evolution universally approaches that of pure Poincaré AdS.

By studying a variety of representative quiver solutions, including Abelian and non-Abelian T-dual backgrounds, quivers with localized flavor groups, and quivers with smeared flavors, we demonstrated how quiver data quantitatively shapes the early-time complexity growth through the geometry-operator-spreading correspondence [13].

Our analysis reveals that holographic Krylov complexity offers a refined probe of quiver dynamics, capturing features beyond what can be inferred from purely radial in-fall. The direction and magnitude of the η-motion depend sensitively on the local slope of the rank functions and on the quiver parameters (P, μ, ν, u_0), providing a dynamical holographic mechanism for how operator growth spreads across gauge nodes. The universality of the late-time regime underscores an appealing physical picture: while early-time complexity retains memory of UV quiver data, the system flows toward an IR regime where operator growth effectively averages over (erases!) the quiver structure. The proper momentum thus encodes both local quiver geometry and emergent universal CFT behavior.

It is worth pointing out here that, while the general connection between the rate of complexity growth and radial momentum was already conjectured [34,35] in the case of AdS and AdS black holes, and argued from using the complexity-volume conjecture in [36] and in [37] and previous work by the same authors, the precise relation (1.1) for *Krylov complexity*, defined and checked

in the case of AdS_3 in global and Poincaré coordinates and the AdS_3 black hole in [13], is on a less strong footing. Thus, we have to understand the extension we proposed here to a more general warped AdS case as a conjecture, based on the understanding of holographic complexity in general. However, the general definition of Krylov complexity in field theory, and in particular in our case, of a Hilbert space containing a quiver space, as well as the regular CFT space, is still lacking, so a specific test of the conjecture is hard to do. A better chance of that stands the case of AdS_2/CFT_1, as then we have a quantum mechanical (as opposed to field theoretic) CFT, so we have a countable (and not continuous) Hilbert space, which we can thus order as $|0\rangle, |1\rangle, |2\rangle, \ldots$, to which in principle we can apply the Lanczos algorithm and Gram-Schmidt orthogonalization with a (non-degenerate!) reference state $|0\rangle$ in order to obtain the Krylov basis, and thus compute the Krylov complexity. Another possibility would be the case that the warped AdS (or a similar gravity dual) is considered in global coordinates, corresponding to a CFT on a sphere, on which we can KK reduce, again obtaining a countable quantum mechanical system. These calculations, possible in principle, we leave to further work.

The results in this paper open several interesting directions. First, it would be natural to extend the present analysis to quiver gauge theories in three and four dimensions. In analogy with recent work on $\mathcal{N} = 4$ SYM [15], one could test whether multi-dimensional quiver directions produce additional channels of operator growth, and whether new forms of damping or universality arise in higher-dimensional holographic flows, for example in the systems of [38–48], etc. Second, it would be valuable to explore backgrounds that combine non-trivial quiver warping with confinement, for example [49–53], etc. Such geometries could clarify how Krylov complexity interpolates between quiver-dominated UV behavior and confining IR phases, potentially offering a new diagnostic of confinement-induced slowdowns or plateaus in operator growth. A further project along the same vein is to examine holographic setups where the probe motion is intrinsically multi-dimensional, requiring evolution not only along r and η but also along an additional internal coordinate. This would provide the first test of Krylov complexity in holographic systems where operator growth explores a genuinely curved, multi-coordinate internal space. Such investigations could reveal novel qualitative spreading patterns and deepen the geometric understanding of complexity in strongly coupled quantum systems.

Overall, our results suggest that top-down holography provides a fertile arena for uncovering the rich dynamical structure of Krylov complexity and its dependence on microscopic field-theory data.

CRediT authorship contribution statement

Ali Fatemiabhari: Investigation; **Horatiu Nastase:** Investigation; **Carlos Nunez:** Investigation; **Dibakar Roychowdhury:** Investigation.

Data availability

No data was used for the research described in the article.

Declaration of competing interest

The authors declare that they have no known competing financial interests or personal relationships that could have appeared to influence the work reported in this paper.

Acknowledgements

For discussions, for comments on the manuscript, and for sharing their ideas with us, we wish to thank: Dmitry Ageev, Nicoló Bragagnolo, Yolanda Lozano, Niall Macpherson, Alfonso Ramallo, Anayeli Ramirez, Ricardo Terrazas. The work of HN is supported in part by CNPq grant 304583/2023-5 and FAPESP grant 2019/21281-4. HN would also like to thank the ICTP-SAIFR for their support through FAPESP grant 2021/14335-0. C. N. is supported by STFC's grants ST/Y509644-1, ST/X000648/1 and ST/T000813/1. DR would like to acknowledge the Mathematical Research Impact Centric Support (MATRICS) grant (MTR/2023/000005) received from ANRF, India.

References

[1] P. Caputa, J.M. Magan, D. Patramanis, Geometry of Krylov complexity, Phys. Rev. Res. 4 (1) (2022) 013041. arXiv:2109.03824, https://doi.org/10.1103/PhysRevResearch.4.013041
[2] Z.-Y. Fan, Generalised Krylov complexity (2023). arXiv:2306.16118
[3] Z.-Y. Fan, Momentum-Krylov complexity correspondence (2024). arXiv:2411.04492
[4] P.-Z. He, Revisit the relationship between spread complexity rate and radial momentum (2024). arXiv:2411.19172
[5] E. Rabinovici, A. Sánchez-Garrido, R. Shir, J. Sonner, A bulk manifestation of Krylov complexity, JHEP 08 (2023) 213. arXiv:2305.04355, https://doi.org/10.1007/JHEP08(2023)213
[6] J. Xu, On chord dynamics and complexity growth in double-scaled SYK, JHEP 06 (2025) 259. arXiv:2411.04251, https://doi.org/10.1007/JHEP06(2025)259
[7] M. Ambrosini, E. Rabinovici, A. Sánchez-Garrido, R. Shir, J. Sonner, Operator K-complexity in DSSYK: Krylov complexity equals bulk length, JHEP 08 (2025) 059. arXiv:2412.15318, https://doi.org/10.1007/JHEP08(2025)059
[8] M.P. Heller, J. Papalini, T. Schuhmann, Krylov spread complexity as holographic complexity beyond Jackiw-Teitelboim gravity, Phys. Rev. Lett. 135 (15) (2025) 151602. arXiv:2412.17785, https://doi.org/10.1103/spcr-jgm6
[9] Y. Fu, H.-S. Jeong, K.-Y. Kim, J.F. Pedraza, Toward Krylov-based holography in double-scaled SYK (2025). arXiv:2510.22658
[10] P. Nandy, A.S. Matsoukas-Roubeas, P. Martínez-Azcona, A. Dymarsky, A. del Campo, Quantum dynamics in Krylov space: methods and applications, Phys. Rept. 1125–1128 (2025) 1–82. arXiv:2405.09628, https://doi.org/10.1016/j.physrep.2025.05.001
[11] E. Rabinovici, A. Sánchez-Garrido, R. Shir, J. Sonner, Krylov Complexity (2025). arXiv:2507.06286

[12] S. Baiguera, V. Balasubramanian, P. Caputa, S. Chapman, J. Haferkamp, M.P. Heller, N.Y. Halpern, Quantum complexity in gravity, quantum field theory, and quantum information science (2025). arXiv:2503.10753
[13] P. Caputa, B. Chen, R.W. McDonald, J. Simón, B. Strittmatter, Spread complexity rate as proper momentum (2024). arXiv:2410.23334
[14] R.N. Das, S. Demulder, J. Erdmenger, C. Northe, Spread complexity for the planar limit of holography, JHEP 06 (2025) 166. arXiv:2412.09673, https://doi.org/10.1007/JHEP06(2025)166
[15] A. Fatemiabhari, H. Nastase, D. Roychowdhury, Holographic Krylov complexity in $\mathcal{N}=4$ SYM (2025). arXiv:2511.19286
[16] A. Fatemiabhari, H. Nastase, C. Nunez, D. Roychowdhury, Holographic Krylov complexity in confining gauge theories (2025). arXiv:2511.22717
[17] Y. Lozano, N.T. Macpherson, C. Nunez, A. Ramirez, AdS_3 Solutions in massive IIA with small $\mathcal{N}=(4,0)$ supersymmetry, JHEP 01 (2020) 129. arXiv:1908.09851, https://doi.org/10.1007/JHEP01(2020)129
[18] Y. Lozano, N.T. Macpherson, C. Nunez, A. Ramirez, 1/4 BPS Solutions and the AdS_3/CFT_2 correspondence, Phys. Rev. D 101 (2) (2020) 026014. arXiv:1909.09636, https://doi.org/10.1103/PhysRevD.101.026014
[19] Y. Lozano, N.T. Macpherson, C. Nunez, A. Ramirez, Two dimensional $\mathcal{N}=(0,4)$ quivers dual to AdS_3 solutions in massive IIA, JHEP 01 (2020) 140. arXiv:1909.10510, https://doi.org/10.1007/JHEP01(2020)140
[20] Y. Lozano, N.T. Macpherson, C. Nunez, A. Ramirez, AdS_3 Solutions in massive IIA, defect CFTs and T-duality, JHEP 12 (2019) 013. arXiv:1909.11669, https://doi.org/10.1007/JHEP12(2019)013
[21] Y. Lozano, C. Nunez, A. Ramirez, S. Speziali, M-Strings and AdS_3 solutions to M-theory with small $\mathcal{N}=(0,4)$ supersymmetry, JHEP 08 (2020) 118. arXiv:2005.06561, https://doi.org/10.1007/JHEP08(2020)118
[22] Y. Lozano, C. Nunez, A. Ramirez, S. Speziali, New AdS_2 backgrounds and $\mathcal{N}=4$ conformal quantum mechanics, JHEP 03 (2021) 277. arXiv:2011.00005, https://doi.org/10.1007/JHEP03(2021)277
[23] Y. Lozano, C. Nunez, A. Ramirez, S. Speziali, AdS_2 Duals to ADHM quivers with Wilson lines, JHEP 03 (2021) 145. arXiv:2011.13932, https://doi.org/10.1007/JHEP03(2021)145
[24] Y. Lozano, C. Nunez, A. Ramirez, $AdS_2 \times S^2 \times CY_2$ Solutions in type IIB with 8 supersymmetries, JHEP 04 (2021) 110. arXiv:2101.04682, https://doi.org/10.1007/JHEP04(2021)110
[25] A. Hanany, E. Witten, Type IIB superstrings, BPS monopoles, and three-dimensional gauge dynamics, Nucl. Phys. B 492 (1997) 152–190. arXiv:hep-th/9611230, https://doi.org/10.1016/S0550-3213(97)00157-0
[26] C. Couzens, Y. Lozano, N. Petri, S. Vandoren, N=(0,4) black string chains, Phys. Rev. D 105 (8) (2022) 086015. arXiv:2109.10413, https://doi.org/10.1103/PhysRevD.105.086015
[27] S. Franco, D. Ghim, S. Lee, R.-K. Seong, D. Yokoyama, 2d (0,2) Quiver Gauge theories and D-Branes, JHEP 09 (2015) 072. arXiv:1506.03818, https://doi.org/10.1007/JHEP09(2015)072
[28] D. Tong, The holographic dual of $AdS_3 \times S^3 \times S^3 \times S^1$, JHEP 04 (2014) 193. arXiv:1402.5135, https://doi.org/10.1007/JHEP04(2014)193
[29] K. Filippas, Holography for 2D $\mathcal{N}=(0,4)$ quantum field theory, Phys. Rev. D 103 (8) (2021) 086003. arXiv:2008.00314, https://doi.org/10.1103/PhysRevD.103.086003
[30] S. Speziali, Spin 2 fluctuations in 1/4 BPS AdS_3/CFT_2, JHEP 03 (2020) 079. arXiv:1910.14390, https://doi.org/10.1007/JHEP03(2020)079
[31] K. Sfetsos, D.C. Thompson, On non-abelian T-dual geometries with ramond fluxes, Nucl. Phys. B 846 (2011) 21–42. arXiv:1012.1320, https://doi.org/10.1016/j.nuclphysb.2010.12.013
[32] Y. Lozano, C. Núñez, Field theory aspects of non-Abelian T-duality and $\mathcal{N}=2$ linear quivers, JHEP 05 (2016) 107. arXiv:1603.04440, https://doi.org/10.1007/JHEP05(2016)107
[33] K. Filippas, C. Núñez, J. Van Gorsel, Integrability and holographic aspects of six-dimensional $\mathcal{N}=(1,0)$ superconformal field theories, JHEP 06 (2019) 069. arXiv:1901.08598, https://doi.org/10.1007/JHEP06(2019)069
[34] L. Susskind, Why do things fall? (2018). arXiv:1802.01198
[35] A.R. Brown, H. Gharibyan, A. Streicher, L. Susskind, L. Thorlacius, Y. Zhao, Falling toward charged black holes, Phys. Rev. D 98 (12) (2018) 126016. arXiv:1804.04156, https://doi.org/10.1103/PhysRevD.98.126016
[36] L. Susskind, Y. Zhao, Complexity and momentum, JHEP 03 (2021) 239. arXiv:2006.03019, https://doi.org/10.1007/JHEP03(2021)239
[37] J.L.F. Barbon, J. Martin-Garcia, M. Sasieta, A generalized momentum/complexity correspondence, JHEP 04 (2021) 250. arXiv:2012.02603, https://doi.org/10.1007/JHEP04(2021)250
[38] M. Akhond, A. Legramandi, C. Nunez, Electrostatic description of 3d $\mathcal{N}=4$ linear quivers, JHEP 11 (2021) 205. arXiv:2109.06193, https://doi.org/10.1007/JHEP11(2021)205
[39] H. Lin, O. Lunin, J.M. Maldacena, Bubbling AdS space and 1/2 BPS geometries, JHEP 10 (2004) 025. arXiv:hep-th/0409174, https://doi.org/10.1088/1126-6708/2004/10/025
[40] D. Gaiotto, J. Maldacena, The gravity duals of N=2 superconformal field theories, JHEP 10 (2012) 189. arXiv:0904.4466, https://doi.org/10.1007/JHEP10(2012)189
[41] C. Núñez, D. Roychowdhury, D.C. Thompson, Integrability and non-integrability in $\mathcal{N}=2$ SCFTs and their holographic backgrounds, JHEP 07 (2018) 044. arXiv:1804.08621, https://doi.org/10.1007/JHEP07(2018)044
[42] C. Nunez, D. Roychowdhury, S. Speziali, S. Zacarias, Holographic aspects of four dimensional $\mathcal{N}=2$ SCFTs and their marginal deformations, Nucl. Phys. B 943 (2019) 114617. arXiv:1901.02888, https://doi.org/10.1016/j.nuclphysb.2019.114617
[43] E. D'Hoker, M. Gutperle, C.F. Uhlemann, Holographic duals for five-dimensional superconformal quantum field theories, Phys. Rev. Lett. 118 (10) (2017) 101601. arXiv:1611.09411, https://doi.org/10.1103/PhysRevLett.118.101601
[44] A. Legramandi, C. Nunez, Holographic description of $SCFT_5$ compactifications, JHEP 02 (2022) 010. arXiv:2109.11554, https://doi.org/10.1007/JHEP02(2022)010
[45] S. Cremonesi, A. Tomasiello, 6d holographic anomaly match as a continuum limit, JHEP 05 (2016) 031. arXiv:1512.02225, https://doi.org/10.1007/JHEP05(2016)031
[46] C. Núñez, J.M. Penín, D. Roychowdhury, J. Van Gorsel, The non-integrability of strings in massive type IIA and their holographic duals, JHEP 06 (2018) 078. arXiv:1802.04269, https://doi.org/10.1007/JHEP06(2018)078
[47] F. Apruzzi, M. Fazzi, D. Rosa, A. Tomasiello, All AdS_7 solutions of type II supergravity, JHEP 04 (2014) 064. arXiv:1309.2949, https://doi.org/10.1007/JHEP04(2014)064
[48] F. Apruzzi, M. Fazzi, A. Passias, A. Rota, A. Tomasiello, Six-dimensional superconformal theories and their compactifications from type IIA supergravity, Phys. Rev. Lett. 115 (6) (2015) 061601. arXiv:1502.06616, https://doi.org/10.1103/PhysRevLett.115.061601
[49] D. Chatzis, A. Fatemiabhari, C. Nunez, P. Weck, SCFT deformations via uplifted solitons (2024). arXiv:2406.01685
[50] D. Chatzis, A. Fatemiabhari, C. Nunez, P. Weck, Conformal to confining SQFTs from holography (2024). arXiv:2405.05563
[51] A. Fatemiabhari, C. Nunez, From conformal to confining field theories using holography, JHEP 03 (2024) 160. arXiv:2401.04158, https://doi.org/10.1007/JHEP03(2024)160
[52] D. Chatzis, M. Hammond, G. Itsios, C. Nunez, D. Zoakos, Universal observables, SUSY RG-flows and holography (2025). arXiv:2506.10062
[53] D. Chatzis, M. Hammond, G. Itsios, C. Nunez, D. Zoakos, Supersymmetric AdS solitons, Coulomb branch flows and twisted compactifications (2025). arXiv:2511.18128